J. Fluid Mech. (1998), *vol.* 359, *pp.* 81–107. Printed in the United Kingdom

From onset of unsteadiness to chaos in a differentially heated square cavity

By PATRICK LE QUÉRÉ AND MASUD BEHNIA†
LIMSI–CNRS, BP 133, 91403 Orsay Cedex, France

(Received 10 October 1994 and in revised form 15 September 1997)

We investigate with direct numerical simulations the onset of unsteadiness, the route to chaos and the dynamics of fully chaotic natural convection in an upright square air-filled differentially heated cavity with adiabatic top and bottom walls. The numerical algorithm integrates the Boussinesq-type Navier–Stokes equations in velocity–pressure formulation with a Chebyshev spatial approximation and a finite-difference second-order time-marching scheme. Simulations are performed for Rayleigh numbers up to 10^{10}, which is more than one order of magnitude higher than the onset of unsteadiness. The dynamics of the time-dependent solutions, their time-averaged structure and preliminary results concerning their statistics are presented. In particular, the internal gravity waves are shown to play an important role in the time-dependent dynamics of the solutions, both at the onset of unsteadiness and in the fully chaotic regime. The influence of unsteadiness on the local and global heat transfer coefficients is also examined.

1. Introduction

Many of the natural convection flows encountered in engineering applications are characterized by length scales or temperature differences such that the corresponding flows are very often turbulent. The past few years have witnessed an increasing number of numerical solutions of the equations describing turbulent natural convection in cavities. In these studies turbulence is accounted for through turbulence models, amongst which the standard k–ϵ model is certainly the most popular. In fact, low-Reynolds-number corrections have to be used because turbulence in natural convection flows is generally weak. This low-Reynolds-number correction is necessary in natural convective flows since the wall region simultaneously provides the driving buoyancy force and acts to damp the turbulence.

On the other hand, direct numerical integrations of the basic unsteady Navier–Stokes equations have generally focused on the instability mechanisms responsible for turning an initially laminar flow into a chaotic one (Haldenwang 1984; Le Quéré 1987; Paolucci & Chenoweth 1989; Penot, Ndame & Le Quéré 1990; Henkes 1990). In short, conclusions of these studies are that, in a differentially heated square cavity with adiabatic top and bottom walls, unsteadiness sets in at a Rayleigh number value slightly less than 2×10^8. Surprisingly, this loss of stability is not due to an instability of the vertical boundary layers but rather to an instability that takes place near the ‘departing’ corners in the detached flow region along the horizontal boundaries. The

---

† Permanent address: School of Mechanical and Manufacturing Engineering, University of New South Wales, Sydney, Australia.

boundary layers themselves become unstable at a slightly higher Rayleigh number and the route to chaos seems to proceed through quasi-periodicity.

In contrast to Rayleigh–Bénard-type configurations, only a few direct simulations of turbulent flows have been performed to date in cavities heated from the sides. A noticeable exception is the pioneering work of Fromm (1971) who first demonstrated, more than 20 years ago, the feasibility of direct simulation of turbulent flow. Another exception is the more recent direct simulation by Paolucci (1990) of two-dimensional turbulent natural convection in a square cavity with adiabatic horizontal walls for a Rayleigh number of 10^{10}. The numerical algorithm was based on a primitive variable formulation and an explicit first-order time-stepping code with second-order spatial differencing on a non-uniform mesh. One of his main findings is that the stratification in the core appears to be significantly reduced compared with the end of the steady laminar regime.

We have performed direct numerical simulations of unsteady and chaotic natural convection in a square cavity with adiabatic horizontal walls, for Rayleigh numbers (Ra) based on the cavity height H from the onset of unsteadiness up to 10^{10}. However, we have focused our attention primarily on Rayleigh numbers below $10^{9.5}$. In this range of Rayleigh numbers, the solutions become increasingly 'turbulent'. In this paper, we discuss the possible transition mechanisms to unsteadiness and chaos. The unsteady features of the flow are presented. Also, we discuss the statistical quantities of interest in the 'turbulent regime', such as the time-averaged temperature and velocity fields, kinetic energy and dissipation and also global heat transfer coefficients. It is hoped that these results will improve our understanding of the fundamentals of the dynamics of turbulent natural convection flows and help constitute data bases that will eventually help the development of better turbulence models. It should be noted that two-dimensional flows, no matter how chaotic they might be, are not really 'turbulent' although we and others recursively use this terminology. Of course, these computations will have to be extended to three-dimensions in the future, when appropriate computational resources become available.

2. Problem description and algorithm

The description of the physical problem is given in de Vahl Davis & Jones (1983). The cavity considered is of height H and its aspect ratio A is assumed to be equal to unity here. It is subjected to a temperature difference ΔT across the vertical isothermal walls while the top and bottom walls are adiabatic. The cavity is filled with a fluid of Prandtl number (Pr) equal to 0.71 corresponding to air. The two-dimensional unsteady Boussinesq equations in primitive variables, which govern the buoyancy-driven flow in the cavity, are made dimensionless with the following reference quantities: $L_r = H$ for length, $V_r = (\alpha/H)/Ra^{1/2}$ for velocity and $t_r = (H^2/\alpha)Ra^{-1/2}$ for time where Ra is the Rayleigh number $Ra = g\beta\Delta T H^3/\nu\alpha$. With these reference quantities, the dimensionless equations are

$$\frac{\partial u}{\partial x} + \frac{\partial w}{\partial z} = 0, \tag{1}$$

$$\frac{\partial u}{\partial t} + u\frac{\partial u}{\partial x} + w\frac{\partial u}{\partial z} = -\frac{\partial P}{\partial x} + \frac{Pr}{Ra^{1/2}}\nabla^2 u, \tag{2}$$

$$\frac{\partial w}{\partial t} + u\frac{\partial w}{\partial x} + w\frac{\partial w}{\partial z} = -\frac{\partial P}{\partial z} + \frac{Pr}{Ra^{1/2}}\nabla^2 w + Pr\Theta, \tag{3}$$

$$\frac{\partial \Theta}{\partial t} + u\frac{\partial \Theta}{\partial x} + w\frac{\partial \Theta}{\partial z} = \frac{1}{Ra^{1/2}}\nabla^2 \Theta, \tag{4}$$

where u and w are the horizontal and vertical velocity components respectively and P the pressure. Θ is the dimensionless temperature defined as $(T - T_r)/\Delta T$, where T_r is the average of the cold and hot wall temperatures.

These equations are integrated by a pseudo-spectral algorithm combining a spatial expansion in series of Chebyshev polynomials with a semi-implicit second-order finite-difference time-marching scheme. The Helmholtz equations arising from time discretization are solved with the tau-method and the partial diagonalization algorithm described in Haidvogel & Zang (1979). The incompressibility condition is treated by the use of an influence matrix technique (Le Quéré & Alziary de Roquefort 1985; Le Quéré 1991). For the sake of brevity, the details of the algorithm are not reproduced here.

3. Results and discussion

3.1. *Symmetry properties*

Before presenting the results, it is worth recalling the following symmetry properties for the configuration under study. It is well known that the equations (1), (2), (3) and (4) with the specified boundary conditions admit solutions which are characterized by a so-called centro-symmetry property. If S is the mapping which consists of a rotation of π with respect to the centre of the computational domain,

$$Sf(x,z,t) = f(1-x, 1-z, t),$$

where f is a two-dimensional field, solutions showing this property have their temperature and velocity fields skew-symmetric with respect to the centre of the computational domain. Their pressure field is symmetrical with respect to the centre of the domain, i.e.

$$S\Theta = -\Theta, \quad Su = -u, \quad Sw = -w, \quad SP = P.$$

Owing to the symmetries of the basis functions $T_l(2x-1) \times T_m(2z-1)$ (where T_l is the lth degree Chebyshev polynomial), this property translates on the spectral coefficients of the temperature, velocity and pressure fields. Any two-dimensional field $f(x,z,t)$ which is skew-symmetric (respectively symmetric) with respect to the centre of the computational domain has all its spectral coefficients f_{lm} with $l+m$ even (respectively $l+m$ odd) identically zero. It is then possible to build simple indicators of this centro-symmetry property by considering, for example, two scalar quantities defined for a field $f(x,z,t)$ as

$$E_s(f) = \sum_{l+m=2p} f_{lm}^2 \quad \text{and} \quad E_a(f) = \sum_{l+m=2p+1} f_{lm}^2.$$

Solutions that satisfy the centro-symmetry property are characterized by $E_s(\Theta) = E_s(u) = E_s(w) = E_a(P) = 0$.

A priori assumption of centro-symmmetry could be used to significantly reduce the computational effort needed (almost by a factor of 2 since only the non-zero spectral coefficients could be solved for in the Helmholtz problems) and also reduces by a factor of 4 the space needed for the storage of the influence matrix. However, in order to allow for possible symmetry-breaking solutions to appear, we chose to compute all the spectral coefficients of the fields and also to systematically monitor the time evolution of the centro-symmetry-breaking indicator $E_s(\Theta)$.

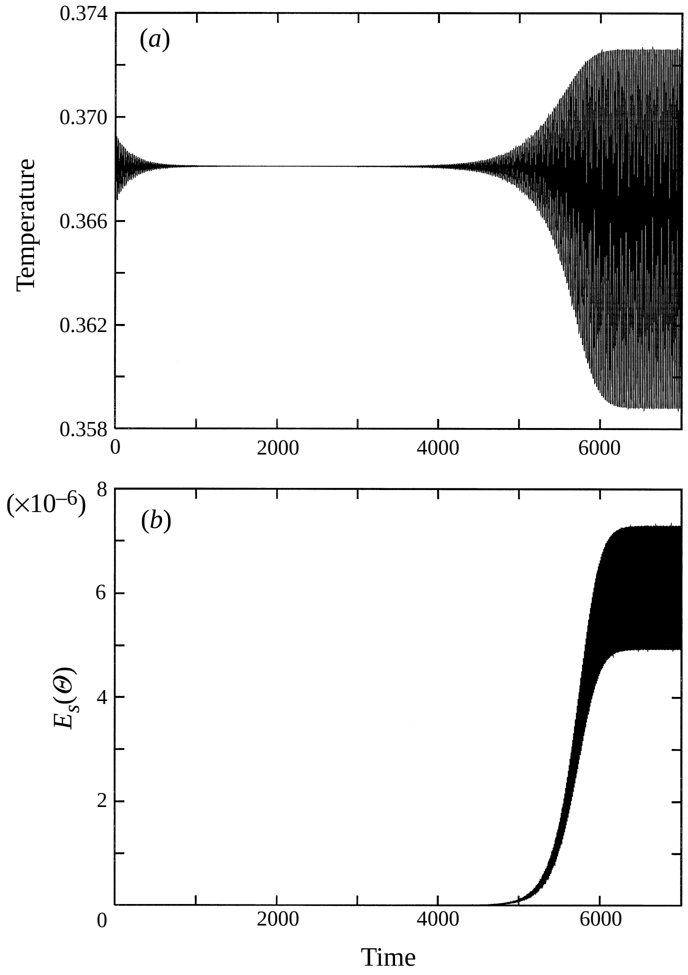

FIGURE 1. (*a*) Time trace of temperature at location $(x, z) = (0.15, 0.88)$, $Ra = 1.84 \times 10^8$. (*b*) Simultaneous evolution of indicator of breaking of centro-symmetry $E_s(\Theta)$. Spatial resolution 72×72, computations performed with $\Delta t = 5 \times 10^{-3}$.

3.2. *First instability mechanism*

3.2.1. *Onset of unsteadiness*

Figure 1(*a*) presents the time trace of the temperature at a given monitoring point for $Ra = 1.84 \times 10^8$. The time integration was started from the steady solution at 1.8×10^8. It is noted that the solution first undergoes damped oscillations and appears to reach a steady state, at least over a time scale of 3000 (in the convective time units used here). This time integration was performed with $\Delta t = 0.005$. This apparently steady solution then starts to show macroscopic oscillations that grow exponentially in time and eventually reaches an asymptotic finite-amplitude periodic state. The period of the oscillation is approximately 22 time units which corresponds to a frequency of 0.045. It is noted that the solution, in this asymptotic periodic state, breaks the centro-symmetry property as indicated by the time evolution of the centro-symmetry-breaking indicator $E_s(\Theta)$ (figure 1*b*). This behaviour can be explained by considering the spectrum of the Jacobian of the operator governing

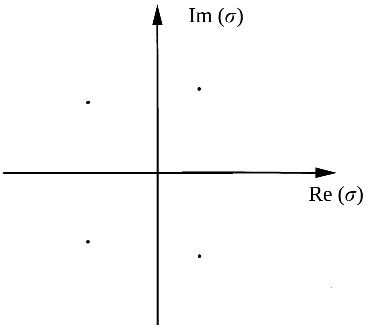

FIGURE 2. Sketch of the eigenvalues of the largest positive real part of the Jacobian in the complex plane.

the time evolution of the solution (with the convention $\partial U/\partial t = \mathscr{L}(U)U$). Since the domain is finite, the spectrum is discrete and we have schematically shown in figure 2 the two pairs of complex eigenvalues of largest real part which account for the observed behaviour. The pair of eigenvalues with negative real parts corresponds to an eigenmode which displays the centro-symmetry property. This mode is still stable and corresponds to the damped oscillations at the very beginning of the time integration. The other pair of eigenvalues corresponds to the unstable eigenmode that breaks the centro-symmetry. Because the initial condition is symmetrical and because the temperature was chosen to be symmetrical (Θ ranges between -0.5 and 0.5), the solution initially stays in a subspace which is orthogonal to this symmetry-breaking unstable eigenmode. However, as we are very close to the critical Rayleigh number, naturally the growth rate of this unstable mode is very small. Furthermore, owing to the above explanation (no perturbation is initially fed on the subspace that breaks centro-symmetry), perturbations that break centro-symmetry have to grow from roundoff errors (10^{-15} on the Cray computer we used) and it therefore takes a very long time for these perturbations to reach a finite-amplitude level and eventually make the solution unsteady and non-symmetrical.

This is further confirmed by performing similar computations for Rayleigh numbers of 1.85×10^8 and 1.86×10^8, starting from the same initial condition. In these cases the growth rates of the unstable centro-symmetry-breaking eigenmode are somewhat larger and at the same time the decay rates of the stable centro-symmetric eigenmode are somewhat smaller. This results in the temperature time signals shown in figure 3, in which the amplification of the symmetry-breaking mode becomes visible before the complete damping of the stable mode has taken place.

In view of the above, the so-called steady solution found for 1.8×10^8 was carefully checked and there appeared to be no indication of this behaviour. Also, the centro-symmetry-breaking solution for 1.84×10^8 was used as initial condition to integrate with smaller values of the Rayleigh number. A finite-amplitude unsteady solution was found for $Ra = 1.83 \times 10^8$, whereas for $Ra = 1.81 \times 10^8$, the solution reverted to a final steady-state solution with $E_s(\Theta)$ tending asymptotically to zero. For $Ra = 1.82 \times 10^8$, the time integration was quite inconclusive, at least for the time period we integrated. It is therefore concluded that the critical Rayleigh number value for the onset of unsteadiness lies between 1.81×10^8 and 1.83×10^8. Further, the corresponding eigenmode and the nonlinear solution break the centro-symmetry property.

It is possible to determine more accurately this critical value by looking at the growth rates of $E_s(\Theta)$ observed for these three time evolutions. Since these quantities

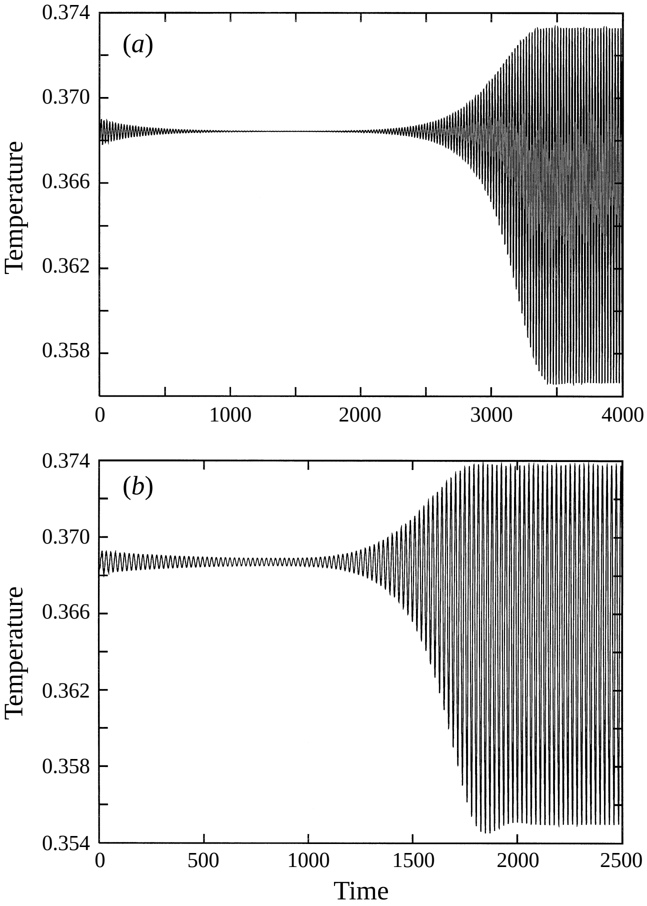

FIGURE 3. Time traces of temperature at location $(x, z) = (0.15, 0.88)$ for $Ra = 1.85 \times 10^8$ (*a*) and $Ra = 1.86 \times 10^8$ (*b*). Spatial resolution 72×72, computations performed with $\Delta t = 5 \times 10^{-3}$.

are initially zero, they grow exponentially in time and their growth rates scale like $(Ra - Ra_c)$. The growth rates, defined as $\mathrm{d}E_s(\Theta)/\mathrm{d}t$, are determined from the time traces shown in figure 4(*a*) as the slopes of the curves for the time length over which $E_s(\Theta)$ grows linearly with t, and are plotted in figure 4(*b*). One observes clearly a linear dependence on $(Ra - Ra_c)$ and extrapolation to zero amplitude yields a critical value of about 1.82×10^8. Computations performed with a larger spatial resolution of $(96, 96)$ confirmed the upper and lower bounds of 1.81×10^8 and 1.83×10^8. We therefore believe that it can be stated, with a reasonable degree of certainty, that the critical value for the onset of unsteadiness is $1.82 \pm 0.01 \times 10^8$.

This value is in good agreement with the value reported by Paolucci & Chenoweth (1989) (1.7×10^8) or Henkes (1990) (1.9×10^8). In fact, it is very likely that Henkes missed the symmetry-breaking bifurcation by not integrating sufficiently long in time, his procedure also being free of initial perturbations on the symmetry-breaking subspace. On the other hand, Paolucci & Chenoweth used a non-Boussinesq formulation with a small value of $\Delta T/T$ (typically 0.001) to satisfy the Boussinesq assumption. They therefore always computed solutions that did not possess exactly the centro-symmetry property. We believe that this is possibly the reason why their solutions

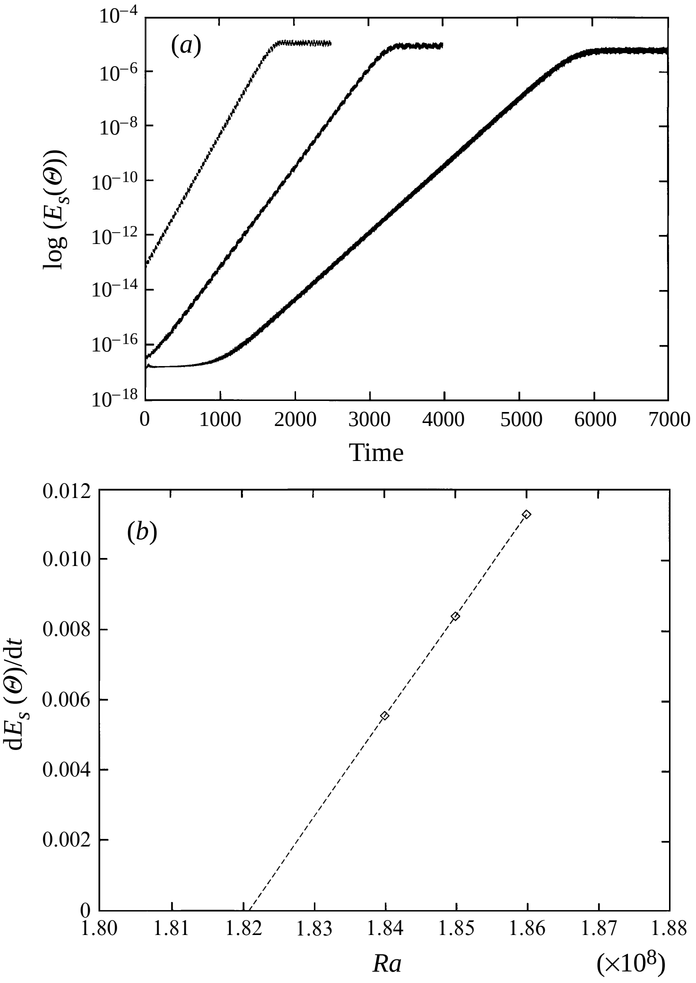

FIGURE 4. (*a*) Time traces of $\log(E_s(\Theta))$ for $Ra = 1.84 \times 10^8$, $Ra = 1.85 \times 10^8$, and $Ra = 1.86 \times 10^8$. (*b*) Evolution of growth rate with Ra.

fall on the symmetry-breaking solution branch. This explanation is at least consistent with the values they obtained (the critical value found by Paolucci & Chenoweth being smaller than that reported by Henkes), regardless of the actual accuracy of either numerical algorithm.

3.2.2. *Structure of fluctuating temperature fields*

A time sequence of the fluctuating temperature field is shown in figure 5. The corresponding time-averaged temperature and flow fields are shown in figure 6. These time-averaged fields were obtained in the usual manner by computing an arithmetic mean of the instantaneous fields over several oscillation periods. The fluctuating temperature was obtained by subtracting this time-averaged temperature field from an instantaneous temperature field. As is quite clear from the figure, the fluctuating temperature field reaches its maximum amplitude in a region that corresponds to the base of the detached flow region which appears along the top horizontal wall in the structure of the steady flow at large enough Rayleigh numbers. It is also apparent

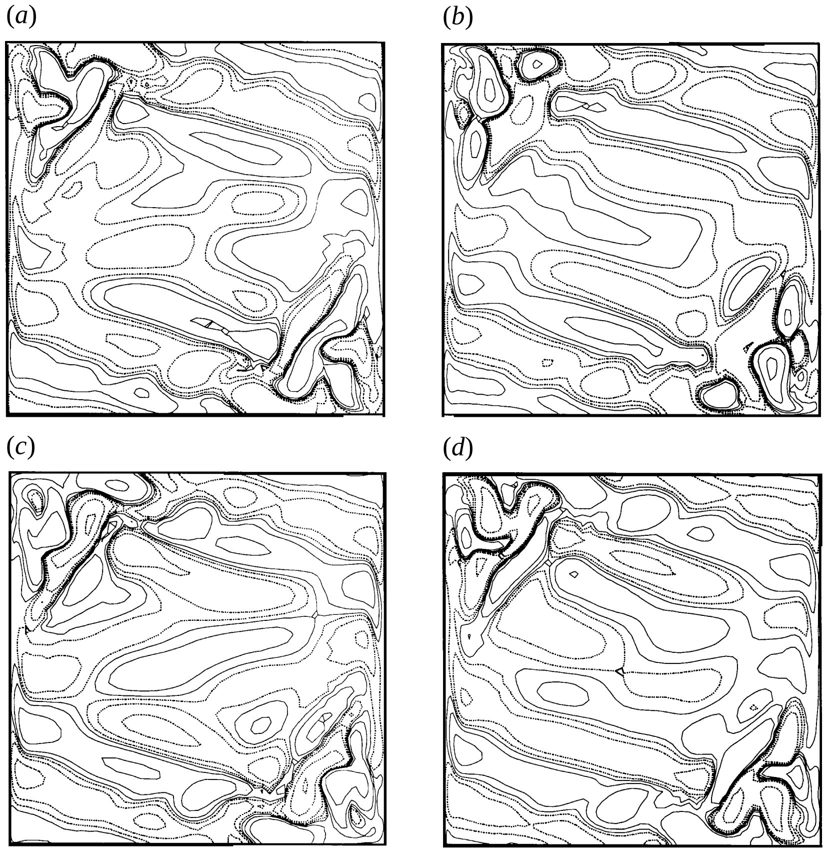

FIGURE 5. (a–d) Time sequence of instantaneous fluctuating temperature fields for $Ra = 1.84 \times 10^8$; spatial resolution 72 × 72; isovalues for the fluctuating field are: $\pm 1 \times 10^{-2}$, $\pm 4 \times 10^{-3}$, $\pm 1 \times 10^{-3}$, $\pm 4 \times 10^{-4}$, $\pm 1 \times 10^{-4}$.

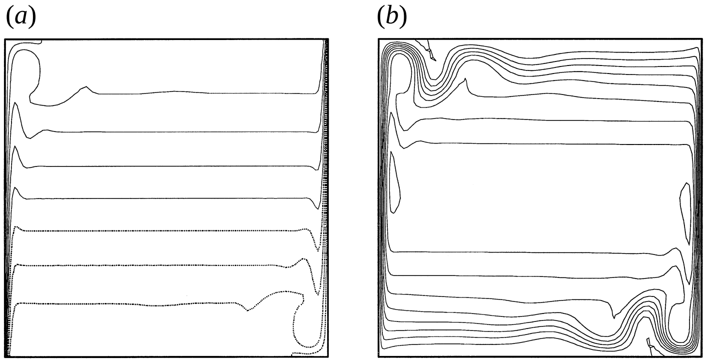

FIGURE 6. Time-averaged temperature (a) and streamfunction fields (b) for $Ra = 1.84 \times 10^8$; spatial resolution 72 × 72; isovalues for the streamfunction are: 0, 0.001, 0.002, 0.003, 0.004, 0.005, 0.006, 0.007, 0.008.

that away from this region the contour lines are inclined at an angle of approximately 20° with respect to the horizontal and they propagate (in time) orthogonally to their direction. We believe that these lines correspond to the wavefronts of internal waves which are shed from the region where the instability mechanism takes place. This is supported by the following argument. It has been shown by Patterson & Imberger (1980) that the stratified core region is capable of sustaining internal gravity waves. These waves are characterized by the Brunt–Väisälä frequency, which in the time unit considered here, is $f_{BV} = (CPr)^{1/2}/2\pi$, where C is the dimensionless stratification in the core region in units of $\Delta T/H$. This frequency f_{BV} corresponds to the frequency of the fundamental mode. Modes with higher wavenumbers are characterized by frequencies smaller than f_{BV} and f_{BV} in fact represents an upper bound for all possible wave patterns. In particular, it is known that if one is to excite a stratified fluid with a particular frequency f, internal waves will be generated only if $f \leqslant f_{BV}$. These waves propagate along a wavevector inclined (with respect to the vertical) at an angle $\theta = \arcsin(f/f_{BV})$ (see Tritton 1988 amongst others). Application of this formula with $f = 0.045$ and $f_{BV} = 0.132$ which corresponds to $C = 1$ yields $\theta = 20°$ matching very closely the observed angle in figure 5. This strongly supports the assertion that internal waves are shed away from the region where the primary instabiliy mechanism takes place. It should also be noted that this phenomenon (the excitation of the internal waves right at the onset of unsteadiness) does not occur in taller cavities where the onset of unsteadiness is due to a travelling wave instability characterized by typical frequencies of 0.5 which indeed is larger than f_{BV} (Le Quéré 1987).

Concerning the physics of the primary instability mechanism, there has not been up to now any definitive explanation of its origin. However, it is noted that the instability takes place at the base of the detached flow region, and it is therefore believed that the instability mechanism is related to this particular flow structure. Armfield (1992) proposed that the existence of the detached flow region is due to a 'thermal blocking effect'. The adiabatic upper (or lower) thermal boundary condition imposed on the flow as it exits the boundary layer causes a temperature overshoot (Armfield 1992) and negative buoyancy forces lead to the plunging of the fluid downward. We find this explanation rather convincing in that it takes into account the high sensitivity of the flow in that region to the thermal boundary conditions at the top or bottom walls. It is indeed noted that there is no detached region in the case of perfectly conducting walls, where the fluid flows smoothly parallel to the horizontal wall.

Concerning the physical mechanism related to the onset of unsteadiness, several hypotheses have been proposed. For instance, Paolucci & Chenoweth (1989) linked the instability to an internal wave breaking mechanism. They argued that the onset of unsteadiness is due to wave breaking of the internal hydraulic jump when the critical Froude number characterizing the jump gets larger than 1.3, which corresponds to a critical Rayleigh number value of $1.6 \times 10^8/PrA^3$. The corresponding value indeed closely matches the observed Ra at which the flow becomes unsteady. They also noted a drop in the frequency of the internal wave motion as the critical Rayleigh is approached. They linked this to an increase of the ratio of the vertical to horizontal wavenumbers of the internal wave pattern.

On the other hand, Armfield (1992) and also Ravi, Henkes & Hoogendoorn (1994) propose that there is no hydraulic jump in these regions. Therefore, the instability mechanism cannot be ascribed to wave breaking, and another explanation has still to be found. In order to get further indications on the nature of the mechanism, we have computed accurately the period of the oscillations in the vicinity of the critical Rayleigh number. These calculations have been very computationally demanding due to the very long oscillation period and the stability criterion which required time integrations on the order of 4000 time steps to complete one oscillation period. The values obtained for several Rayleigh numbers are given in table 1. The solutions

Ra	# time steps	Period Π	$\Pi \times Ra^{-2/3}$	$\Pi \times Ra^{-3/4}$
1.82×10^8	4289	21.445	6.677 (−5)	1.3686 (−5)
1.83×10^8	4303	21.515	6.675 (−5)	1.367 (−5)
1.84×10^8	4320	21.60	6.677 (−5)	1.367 (−5)
1.85×10^8	4335	21.675	6.676 (−5)	1.372 (−5)

TABLE 1. Variation of period with Ra at onset of unsteadiness. Computations performed with spatial resolution (96, 96) and time step $\Delta t = 0.005$.

for increasing values of Ra were obtained by using the solution for the immediately lower value of Ra as initial condition. All these solutions break the centro-symmetry property and thus belong to the same branch of solutions. These values clearly show that the dimensionless period increases with Ra and a power-law fit yields an exponent α of between 2/3 and 3/4. The dimensional period of oscillation thus scales like ΔT^{δ} with $\delta = \alpha - 1/2 \geqslant 1/6$. Hence, the dimensional oscillation period increases with ΔT, a somewhat curious result. It is also apparent, although not quantified, from the results of Henkes (1990) that, in the vicinity of the critical point, the dimensionless frequency decreases with increasing Ra. In contrast, the internal wave breaking mechanism proposed by Paolucci & Chenoweth 1989 would be characterized by a dimensional frequency scaling of $\Delta T^{1/2}$. This does not agree with our findings, and thus seems to rule out the internal wave breaking mechanism.

An understanding of the mechanism could perhaps be obtained from the examination of the structure of the fluctuating field, which in our opinion always displays a signature characteristic of the underlying instability. A close-up view of the fluctuating temperature field in the upper left corner is shown in figure 7. Unfortunately, this structure is not reminiscent of any pattern characteristic of the classical known types of instabilities. Recently, it has been suggested that this instability could be a Kelvin–Helmholtz-type instability of the jet-like structure emerging from the vertical boundary layers (Janssen & Henkes 1994). This was supported by an examination of the spatial structure of the fluctuating field obtained for various aspect ratios and Prandtl numbers, which allowed them to relate more clearly the instability pattern to a Kelvin–Helmholtz-type instability than in the present case. A definitive explanation would require linking the characteristic local Reynolds and Richardson numbers of the local shear flow to the imposed macroscopic parameters which are the Rayleigh and Prandtl numbers and aspect ratio. This remains to be done. Another specific feature of the present instability mechanism is the large variation of its growth rate with Ra in the vicinity of Ra_c. This manifests itself in the fact that for Ra values only slightly supercritical the time traces which are obtained are highly nonlinear. Such a behaviour is characteristic of thermal-type instabilities and it is very likely that the present instability mechanism gets a substantial part of its energy from buoyancy forces.

3.2.3. *Discussion of the breaking of symmetry*

That the onset of instability is associated with breaking of the centro-symmetry is fully explained by bifurcation theory in the presence of symmetries (Chossat 1984). In a space of divergence-free vector fields, the two-dimensional Navier–Stokes equations

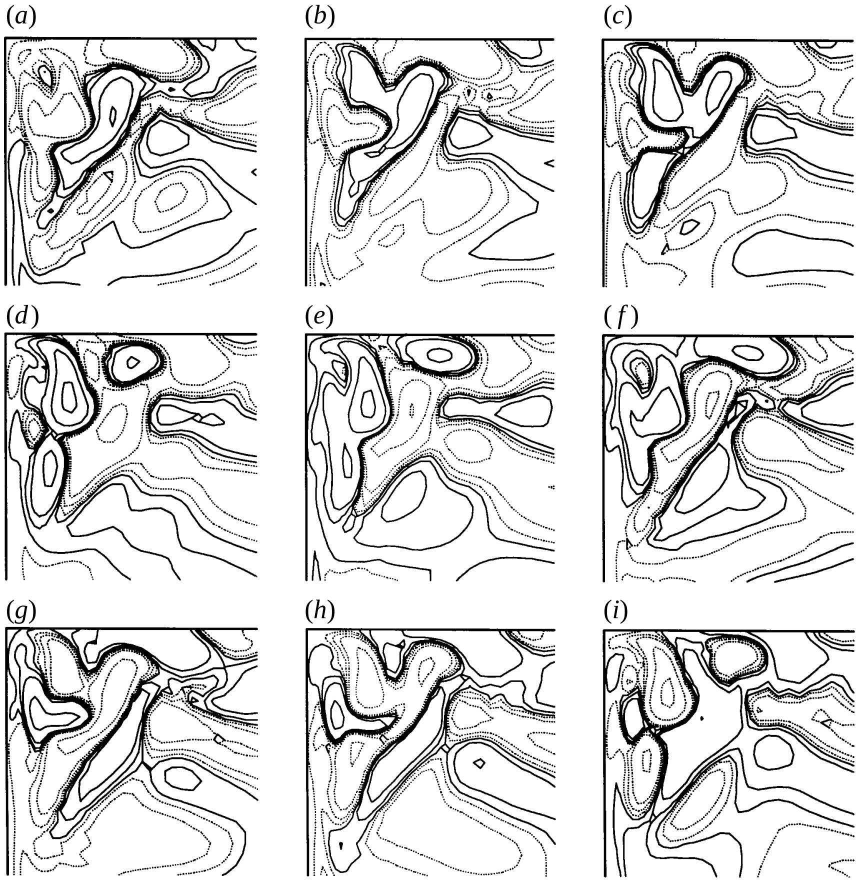

FIGURE 7. (*a–i*) Time sequence of fluctuating temperature field for $Ra = 1.84 \times 10^8$; time interval between two plots = 5; spatial resolution 72 × 72; only upper left corner of the cavity is shown. Isovalues are: $\pm 1.5 \times 10^{-2}$, $\pm 1 \times 10^{-2}$, $\pm 5 \times 10^{-3}$, $\pm 2 \times 10^{-3}$, $\pm 1 \times 10^{-3}$, $\pm 5 \times 10^{-4}$.

with the Boussinesq approximation can be written

$$\frac{\partial U}{\partial t} = \mathscr{L}(U)U, \tag{5}$$

where U represents the three fields $(u, w, \Theta)^t$ defined on Ω and $\mathscr{L}$ is the nonlinear evolution operator. It is a classical result that $\mathscr{L}$ is equivariant with respect to all symmetries S such as the one that was introduced previously, that is $\mathscr{S}\mathscr{L} = \mathscr{L}\mathscr{S}$. This result is also true for the linearized evolution operator governing the evolution of small disturbances v about a steady solution V of (5):

$$\frac{\partial v}{\partial t} = \mathscr{L}_U(V)v$$

where $\mathscr{L}_U$ is the Frechet derivative of $\mathscr{L}$. If V undergoes a supercritical Hopf bifurcation, there exists a complex pair of eigenvalues $(\sigma, \overline{\sigma}) = \mathrm{i}(\omega, -\omega)$ of $\mathscr{L}_U$ which crosses the imaginary axis, associated with a pair of complex eigenfunctions $(v, \overline{v})$. One thus has $\mathscr{L}_U S v = S \mathscr{L}_U v = \sigma S v$ which means that Sv is also an eigenfunction of $\mathscr{L}_U$ associated with eigenvalue σ. If the eigenspace associated with σ is of dimension 1 (which is most often the case), that is σ is a simple eigenvalue of $\mathscr{L}_U$, one thus

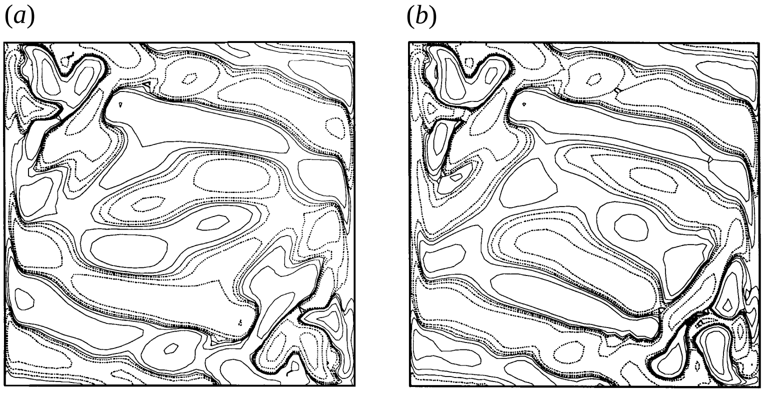

FIGURE 8. Instantaneous fluctuating temperature fields for $Ra = 2 \times 10^8$; (*a*) shows the solution which exhibits centro-symmetry; spatial resolution 72×72; isovalues are: $\pm 1. \times 10^{-2}$, $\pm 4 \times 10^{-3}$, $\pm 1 \times 10^{-3}$, $\pm 4 \times 10^{-4}$, $\pm 1 \times 10^{-4}$, negative isovalues are shown as dotted lines.

has $Sv = \mu v$. Since $S^2 = I$, it follows that $\mu^2 = 1$ or $\mu = \pm 1$. Thus either $Sv = v$ or $Sv = -v$, denoting that either v possesses the centro-symmetry property or on the contrary v is symmetrical with respect to the centre of Ω. Now if the Hopf bifurcation is supercritical, for small supercritical values the bifurcated solution can be written

$$U(x,t) = V(x) + \epsilon \mathscr{R}(\exp(2\pi i\omega t)v + \exp(-2\pi i\omega t)\bar{v}) + O(\epsilon^2)$$

where $\epsilon = (Ra - Ra_c)^{1/2}$.

If v is such that $Sv = -v$, then it immediately follows that $SU(x,t) = -U(x,t)$ and the bifurcated solution continues to show the centro-symmetry property at any time. On the other hand if $Sv = v$ then the bifurcated solution loses the centro-symmetry property. However

$$U\left(x, t + \frac{\pi}{\omega}\right) = V(x) - \epsilon \mathscr{R}(\exp(i\omega t)v + \exp(-i\omega t)\bar{v}) + O(\epsilon^2)$$

and

$$SU\left(x, t + \frac{\pi}{\omega}\right) = -U(x,t).$$

In the linear approximation, the bifurcated solution thus continues to show the centro-symmetry properties shifted in time by half the oscillation period. This is no longer true of the fully nonlinear solution.

3.3. *Unsteady solutions for* $Ra = 2 \times 10^8$

When computing solutions for large values of the Rayleigh number, it is customary to use solutions obtained for slightly smaller values of the parameter as initial condition. Whereas the final solution does not usually depend on the initial condition in particular in the steady regime, one can anticipate non-unique solutions when the solutions become time-dependent. When computations were performed for $Ra = 2 \times 10^8$, using either the steady solution found for 1.8×10^8 or one instantaneous centro-symmetry breaking solution for 1.9×10^8 as initial conditions, it was discovered that the asymptotic solutions were not the same, although the transient features look very similar. Both final asymptotic solutions are periodic in time and exhibit oscillations with similar amplitudes and periods differing by less than 2% which makes it very difficult to differentiate them merely from this criterion. One of the solutions (the one which was obtained starting from a centro-symmetry breaking

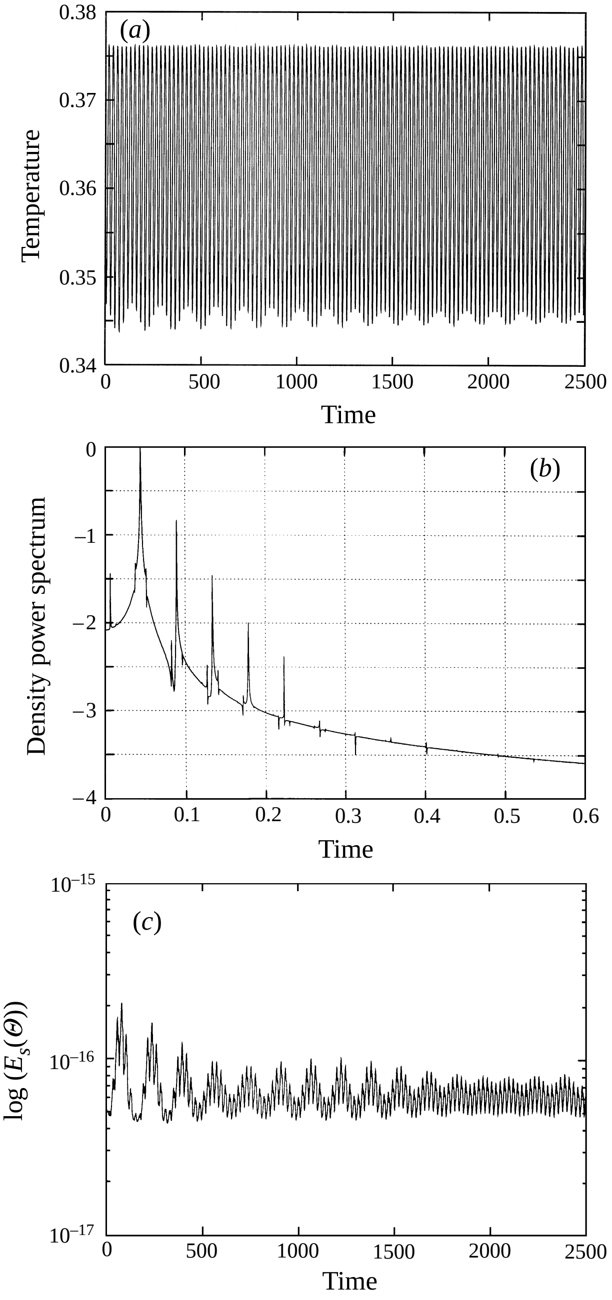

FIGURE 9. (*a*) Time trace of temperature at location $(x, z) = (0.15, 0.88)$, $Ra = 2 \times 10^8$ for centro-symmetric solution. (*b*) Corresponding density power spectrum. (*c*) Simultaneous time evolution of $\log(E_s(\Theta))$. Spatial resolution 72×72, computations performed with $\Delta t = 5 \times 10^{-3}$.

solution) is characterized a period of 4414 time steps of 0.005 each (a period of 22.07) whereas the other has a period of 4480 time steps (a period of 22.4).

These two solutions differ essentially by their spatial structure and figure 8 presents two instantaneous fluctuating temperature fields for each of these solutions. These plots clearly show that one fluctuating field possesses the centro-symmetry property while the other does not. One of these solutions belongs to the first branch of solutions that was discussed in the previous paragraph whereas the other one belongs to a second branch of solutions and corresponds to the eigenmode that was still stable on the sketch of figure 2 and which has become unstable upon increasing the Rayleigh number as could be expected. It was carefully checked that in either case the asymptotic time behaviour of $E_s(\Theta)$ was reached and that both solutions can be considered as stable over very long, not to say infinite, integration times (see in particular the time trace of $E_s(\Theta)$ shown in figure 9*c*). We can therefore conclude that there exist at least two unsteady periodic solutions to the Boussinesq equations for a Rayleigh value of 2×10^8. By decreasing the *Ra* value, starting from the centro-symmetric solution obtained for 2×10^8 as initial condition, we could obtain periodic solutions on that centro-symmetric branch down to *Ra* values slightly less than 1.9×10^8.

It is also of interest to examine the time signals of pointwise quantities during the transient evolution. Figure 9(*a*) presents such a time trace for the solution computed for $Ra = 2 \times 10^8$ using the steady solution obtained for $Ra = 10^8$ as the initial condition (the time evolution for the other solution is very similar). It is noted that the time interval shown corresponds to the final 2500 time units of a total integration time of 5000, a very long integration period indeed. This required approximately 20 hours of CPU time on a Cray-2. It is seen from the figure that the asymptotic time evolution is made up of two frequencies, which show up very clearly in the density power spectrum (figure 9*b*). The primary frequency, which is low itself (about 0.045), is modulated by a yet lower frequency, which seems to die out very slowly. The origin of this very low frequency is somewhat obscure. It could correspond directly to the characteristic frequency of another eigenmode, with its pair of complex eigenvalues characterized by small negative real parts and which therefore requires a long damping time. It could also come from the nonlinear interactions of two unstable modes with slightly different oscillation periods, as could be the case if the solution was made up of the two distinct eigenmodes found previously. This latter explanation can probably be ruled out for several reasons. First, the solution is centro-symmetric and there is therefore no component on the unstable centro-symmetry breaking subspace. Second, the density power spectrum of the signal (figure 9*b*) shows only one peak close to 0.045, which seems to exclude the possibility of two centro-symmetric eigenmodes of slightly different frequencies. It is therefore very likely that this damped low frequency actually corresponds to a pair of eigenvalues with very small imaginary part (and small negative real part) associated with an eigenmode. It would be of course of great interest to determine the spatial structure of this eigenmode to understand its physical origin.

3.4. *Onset of travelling waves*

As shown by others (e.g. Paolucci & Chenoweth 1989; Henkes 1990), the travelling wave instability starts soon after the first instability mechanism. For $Ra = 3 \times 10^8$, the asymptotic time trace at a point located close to the wall in the upper left corner is displayed in figure 10(*a*). This signal is evidently made up of several components oscillating at different frequencies. The modulation of period approximately 20 corresponds to the primary instability mechanism already discussed. The high-frequency signal is attributed to travelling waves in the boundary layer. These travelling waves are clearly seen in figure 11 which presents a time sequence of the entire fluctuating temperature field obtained in the manner already described. The travelling wave

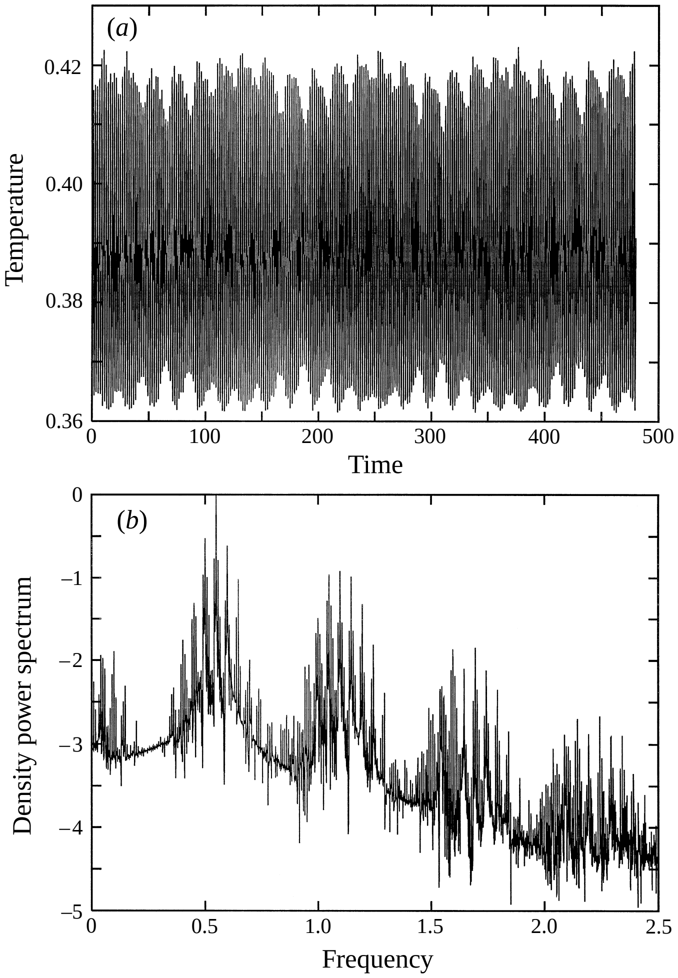

FIGURE 10. (*a*) Time trace of temperature at location $(x, z) = (0.17, 0.93)$, $Ra = 3 \times 10^8$; Spatial resolution 96×96, computation performed with $\Delta t = 4 \times 10^{-3}$. (*b*) Corresponding density power spectrum; sampling of 8192 points over interval of 1638.4.

period is 1.82 which is about 10 times smaller than the period of the primary instability mechanism. Again, the fluctuating temperature fields show internal waves that propagate in the core region at an angle of 20° (from horizontal) approximately. The structure of the temperature fluctuations in the corner regions is now very complex and the structures that come from the travelling waves in the boundary layers interact very strongly with the structures due to the primary instability mechanism (see the close-up in figure 12). Also apparent in the time trace is a modulation of very long period approximately equal to 120.

The corresponding density power spectrum is displayed in figure 10(*b*). The peak frequency corresponds to the travelling wave frequency f_2 and is equal to 0.55. The frequency of the primary instability f_1 is equal to 0.048. Several peaks $mf_1 + nf_2$ with low values of m and n are visible and illustrate nonlinear interactions between these two independent oscillators which are localized at neigbouring positions. The lowest significant frequency present in the signal is approximately equal to 0.007, and corresponds to the very long-period modulation observed in the time trace. It is unclear

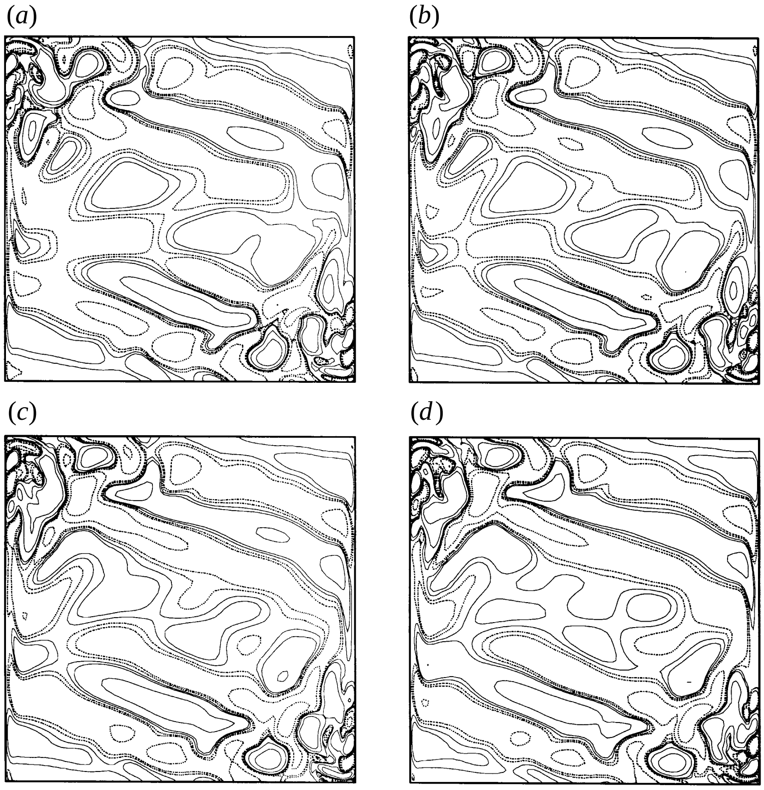

FIGURE 11. (*a–d*) Time sequence of fluctuating temperature field for $Ra = 3 \times 10^8$; time interval between two plots = 5; isovalues are: $\pm 4 \times 10^{-2}$, $\pm 3 \times 10^{-2}$, $\pm 2 \times 10^{-2}$, $\pm 1 \times 10^{-2}$, $\pm 5 \times 10^{-3}$, $\pm 2 \times 10^{-3}$, $\pm 1 \times 10^{-3}$.

whether it also corresponds to a linear combination $mf_1 + nf_2$ with large m and n or to a third independent frequency f_3. We favour this latter explanation and believe that it is indeed due to the triggering of an independent oscillator corresponding to a third instability mechanism. This is supported by two arguments. First, this frequency closely matches the very low frequency that was found in the asymptotic time evolution observed for 2×10^8, which corresponded then to a weakly damped oscillator. Increasing the Ra value to 3×10^8 would have made that oscillator unstable. Second, we believe that it does not come from nonlinear interactions between the primary instability mechanism and the travelling waves. This is supported by the fact that the travelling wave frequency f_2 can only be seen in the time traces of monitoring points located in the downstream parts of the boundary layers and is not present in some regions of the flow, whereas the two other frequencies f_1 and f_3 are always seen in the time traces of pointwise quantities whatever their location in the flow field. The time evolution of the solution for $Ra = 3 \times 10^8$ would thus be characterized by three independent frequencies and it could already be weakly chaotic as suggested by the density power spectrum shown in figure 10(*b*) or by a Poincaré section (figure 13).

3.5. *Chaotic solutions*

In addition to the above results we have also obtained asymptotic solutions for $Ra = 10^9$, $10^{9.5}$ and 10^{10}. The computations at the latter value of the Rayleigh number were performed after the submission of the initial version of this paper and

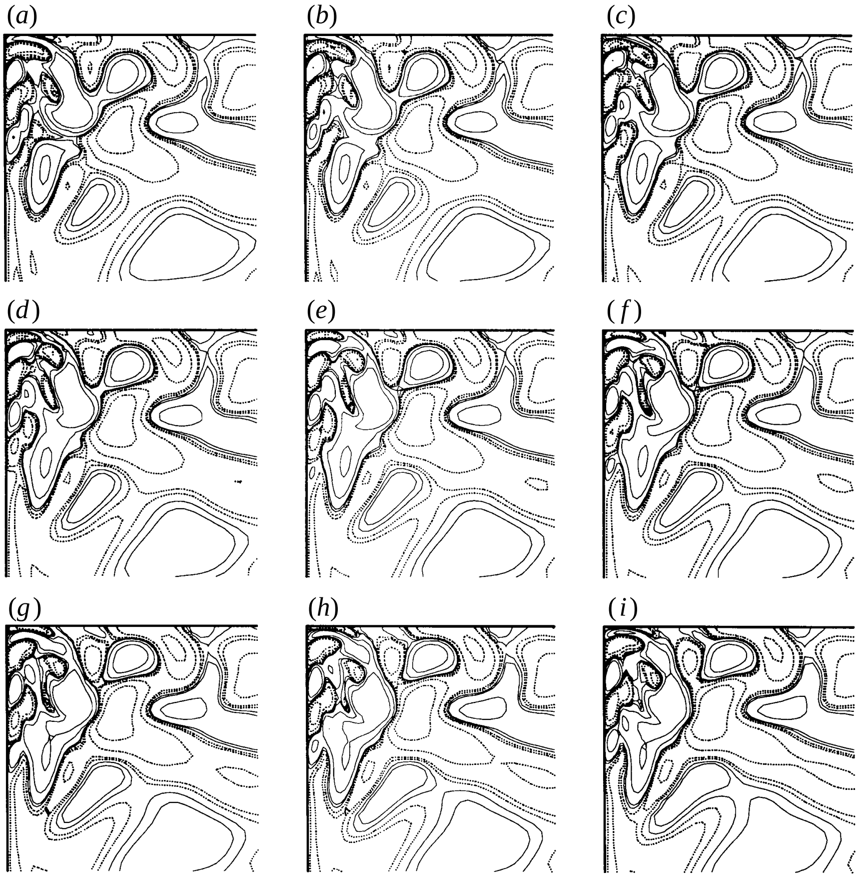

FIGURE 12. (*a–i*) Time sequence of fluctuating temperature field for $Ra = 3 \times 10^8$; time interval between two plots = 2.5; close-up of area $0 \leqslant x \leqslant 0.5, 0.5 \leqslant z \leqslant 1.$ is shown; isovalues are: $\pm 4 \times 10^{-2}$, $\pm 3 \times 10^{-2}$, $\pm 2 \times 10^{-2}$, $\pm 1 \times 10^{-2}$, $\pm 5 \times 10^{-3}$, $\pm 2 \times 10^{-3}$, $\pm 1 \times 10^{-3}$.

are included here to follow a suggestion made by one of the referees, in order to allow for a direct comparison with corresponding simulations by Paolucci (1990). These results have been presented elsewhere (Le Quéré 1994) and will not be discussed in as much detail as the lower values. In these computations we have focused our attention on *Ra* well above the onset of chaos in order to investigate directly the dynamics and statistics of such solutions. For these parameter values, the flow is considered to be weakly turbulent. For each Rayleigh number considered, solutions were integrated using a solution corresponding to a smaller Rayleigh number as the initial condition. For these computations, one needs to ascertain that the integration time is long enough so that the transient effects due to the sudden change of *Ra* are eventually 'forgotten', ensuring that a true statistically steady state has indeed been reached. Table 2 shows the time-step values, spatial resolutions and total integration times of the solutions computed. Note that these times are given in units of convective scale $(H^2/\alpha)Ra^{-1/2}$ and should be divided by $Ra^{1/2}$ to be cast in units of thermal diffusion scale ($= H^2/\alpha$). In particular, for $10^{9.5}$ and 10^{10} integration was carried out for approximately 0.003 units of thermal diffusion time whereas, for instance, Paolucci (1990) stopped his computation around 0.001 starting from rest.

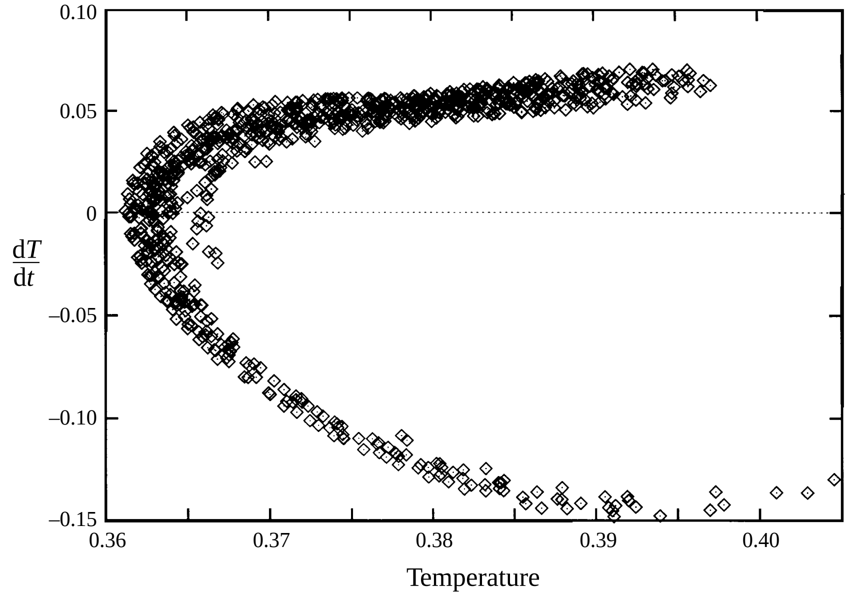

FIGURE 13. Poincaré section of flow for $Ra = 3 \times 10^8$; the Poincaré section is made of the temperature and its time derivative at $(x, z) = (0.17, 0.93)$ conditioned by the Nusselt number. Computation performed with spatial resolution 96×96 and $\Delta t = 4 \times 10^{-3}$. The Poincaré section is made of approximately 1000 points which required integrating over 500 000 time steps.

Ra	$N \times M$	Δt	Total time
10^8	72×72 tau		
3×10^8	96×96 tau		
10^9	193×193 tau	2.0×10^{-3}	600.0
$10^{9.5}$	256×385 tau	1.0×10^{-3}	400.0
10^{10}	256×320 coll.	2.0×10^{-3}	300.0

TABLE 2. Computation parameters: spatial resolution $N \times M$ and algorithm, time step Δt.

The time needed to reach the asymptotic state is not known *a priori*. Patterson & Imberger (1980) have shown that, in the convection-dominated laminar regime, the time to achieve steady state is of the order of $0.1 \times Ra^{1/2}$ in the time unit considered here. This very long time scale is the time needed to damp, through diffusion and viscous effects, the internal gravity waves sustained by the stratified core region which have been generated in the transients following the sudden change in Ra value. It is clear that if the time needed here were of the same order as this time scale, the statistically accurate steady state would be out of reach. However, because the solution is very chaotic and shows large-amplitude fluctuations which enhance long-scale mixing, it is clear that the time required to achieve asymptotic behaviour is decreased. This is also due to the fact that as was shown above and will be confirmed below, internal wave motion is intrinsically part of the asymptotic time behaviour, and hence the long time scale needed to damp out these waves becomes irrelevant in the present chaotic flow regime.

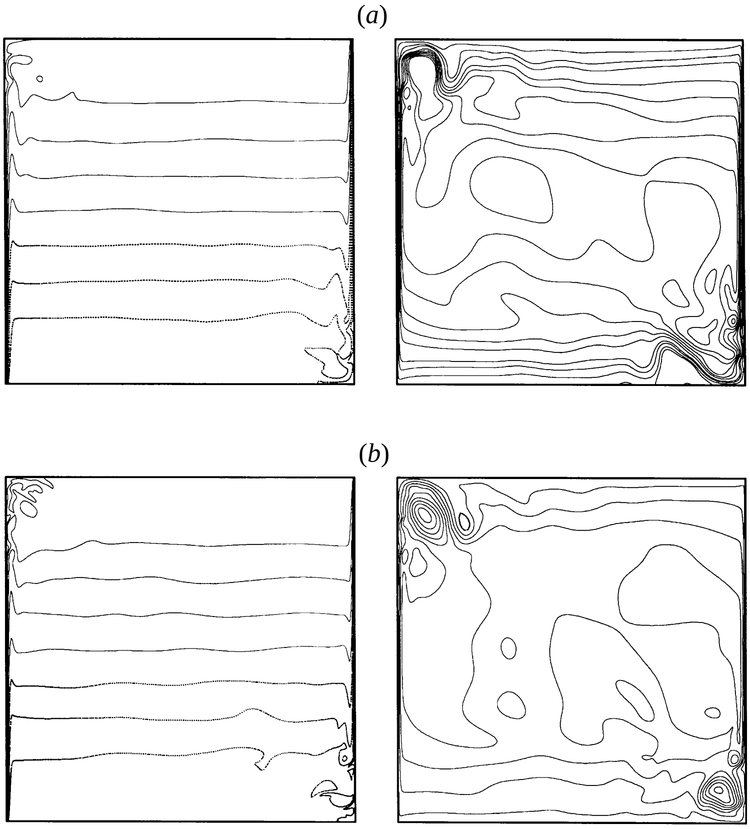

FIGURE 14. Instantaneous temperature (left) and flow (right) fields for $Ra = 10^9$ (*a*), $Ra = 10^{9.5}$ (*b*).

3.5.1. *Flow structures*

Instantaneous flow structure

As mentioned earlier, at these parameter values, the flow exhibits large-amplitude unsteady fluctuations. Typical instantaneous flow and temperature fields are displayed in figure 14 for the two lowest Rayleigh numbers. They show that, as expected, the flow is increasingly disorganized and chaotic as the Rayleigh number increases. In particular, it is seen that, for the higher *Ra*, the travelling waves have grown to the point where they totally disrupt the boundary layer, which at times separates from the wall. These zones correspond to the formation of hook-like structures (figure 14) in the temperature field which characterize buoyancy-driven boundary layers in the transition regime. These hook-like structures are due to strong vortices that spin clockwise (in the hot boundary layer) very fast compared to their upward velocity and which eject hot fluid and entrain colder fluid. From the flow structure, it is also clear that the core region exhibits large-scale unsteady structures appearing as wave-like patterns on the isotherms in the core region of the cavity.

The motion in the cavity core is due to the internal wave activity. First, as already described, in this configuration internal waves get excited at the onset of unsteadiness because the frequency of the primary instability mechanism is smaller than the natural Brunt–Väisälä frequency. As long as the excitation is mono-periodic the internal wave pattern responds to this excitation by displaying the pattern shown in figure 5 or

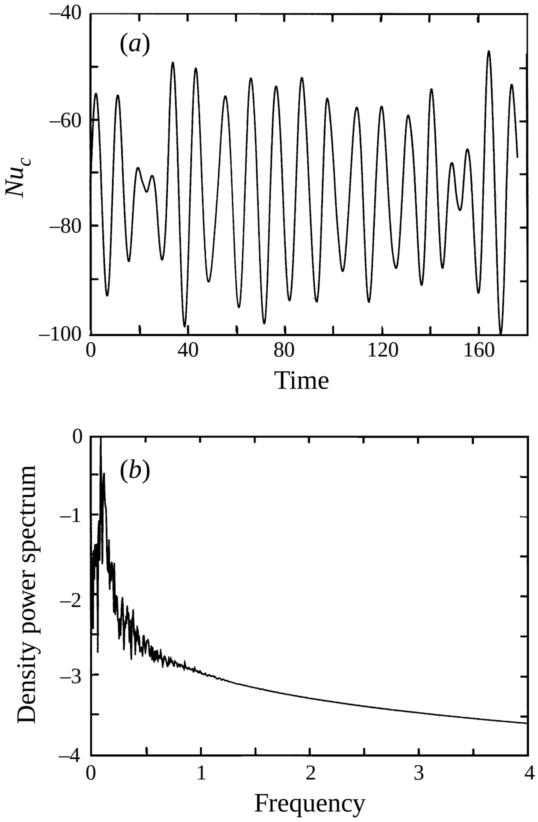

FIGURE 15. Time trace of Nusselt number Nu_c (*a*) and its density power spectrum (*b*) for $Ra = 10^{9.5}$; density spectrum is obtained from a time series of 8192 points over a time interval of 163.84. Spatial resolution 256 × 384, computation performed with $\Delta t = 5 \times 10^{-3}$.

figure 8. At higher values of Ra, the flow becomes chaotic and is then characterized by a broad-band spectrum. The wave pattern in the core should therefore not be expected to be so regular and it is very likely that it oscillates according to various modes characterized by several wavenumbers in the vertical and horizontal directions. As was shown by Thorpe (1968), in a closed cavity, internal waves can build standing patterns which are characterized by their number (n, p) of half-wavelengths in the vertical and horizontal directions, respectively. The frequency of the (n, p) mode is

$$\sigma_{np}^2 = \frac{f_{BV}^2}{1 + n^2/(p^2 A^2)},$$

where A is the aspect ratio of the linearly stratified core region. In our time unit, the dimensionless Brunt–Väisälä frequency is $f_{BV} = (CPr)^{1/2}/(2\pi)$, where C is the dimensionless stratification measured in units of $\Delta T/H$. Taking $C = 1$ (see figure 16) gives $f_{BV} = 0.134$. It is clear from the shapes of the isotherms in the core that there exists at least two or three wavelengths of horizontally propagating internal waves in the core, which seem to propagate from the hot wall towards the cold wall in the upper part of the core and from the cold wall to the hot wall in the bottom part of the core. The wave pattern in the vertical direction is less clear. However, the characteristic frequency of any standing wave pattern should be between $f_{BV}/\sqrt{2}$

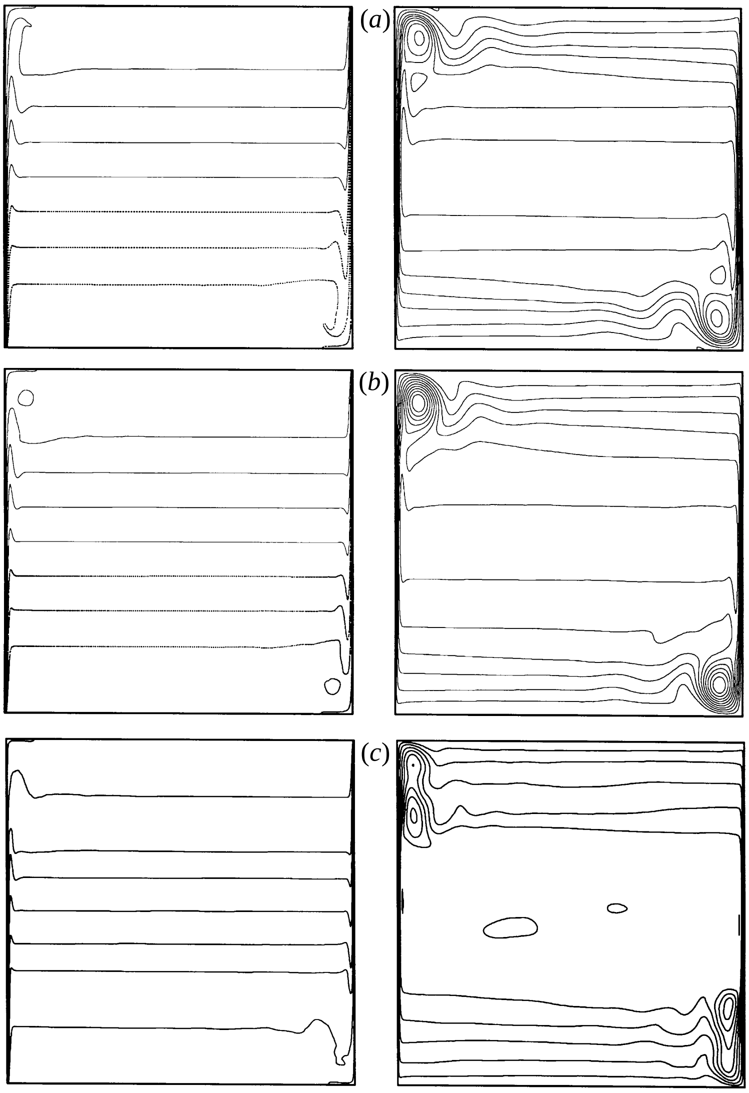

FIGURE 16. Time averaged temperature (left) and flow (right) fields for $Ra = 10^9$ (*a*), $Ra = 10^{9.5}$ (*b*), $Ra = 10^{10}$ (*c*). Streamline isovalues for $Ra = 10^{9.5}$ are: 0.0005 (0.0005) 0.005.

and f_{BV}. It is known that the internal wave oscillations are well characterized by the time evolution of the mean Nusselt number Nu_c through the vertical mid-plane (figure 15*a*). Its density power spectrum shows a dominant frequency of 0.098 which falls within the range predicted. We thus believe that it is clearly demonstrated that internal wave oscillations are intrinsically part of the asymptotic flow regime, even though it seems that one should not anticipate a unique and well-defined wave pattern. Video-animations made from the results also very clearly show the phenomenon and support this assertion.

Time-averaged flow structure

The time-averaged solutions integrated over a long period are displayed in figure 16. The usual typical flow features, i.e. thin vertical boundary layers and a stratified core region as well as corner recirculations, are evident.

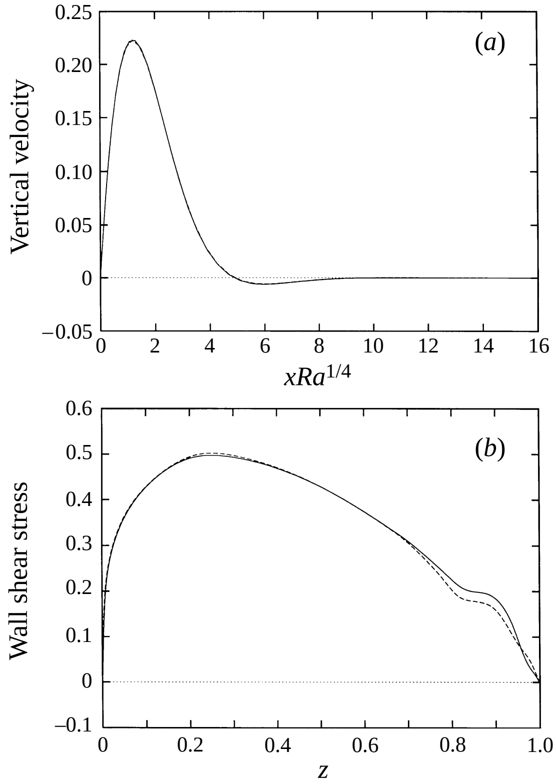

FIGURE 17. (*a*) Vertical velocity profiles at mid-height and (*b*) wall shear stress for $Ra = 10^9$ (solid line) and $Ra = 10^{9.5}$ (dashed line). The vertical velocity profile is plotted vs. $x \times Ra^{1/4}$. The shear stress is defined as $Ra^{-1/4}\partial w/\partial x$.

It is also noted that whilst the time-averaged solution for 10^9 shows little difference from the well-known structure corresponding to the end of the steady laminar regime, the solutions for $10^{9.5}$ and 10^{10} increasingly depart from this structure. In particular, the corner recirculation zones exhibit a much stronger flow. This is confirmed by the maximum values of the streamfunction in these recirculation regions which increases with *Ra*, whereas in the present units, the flow rate in the boundary layer decreases like $Ra^{-1/4}$, as confirmed by the plots of the velocity profile at the mid-cavity height (figure 17*a*). It is also noted that there is a sudden thickening of the boundary layer along the hot wall around $z \simeq 0.7$ (and symmetrically in the cold boundary layer), which corresponds to a sharper decrease of the wall shear stress followed by a plateau corresponding to a locally parallel flow and constant velocity maximum (figure 17*b*). On the other hand, the temperature fields show that the core regions still display uniform stratification for all *Ra* values. However, it is seen that while for the two lowest *Ra* values, the dimensionless stratification remains very close to 1 in units of $\Delta T/H$, it increases to 1.1 for the highest *Ra*. This is in disagreement with the 'asymptotic' stratification (i.e. 0.38) reported by Paolucci in the 10^{10} case. Further, in a companion study (Xin & Le Quéré 1995) performed in a cavity of aspect ratio 4 for Ra_H up to 10^{10}, it was also found that the stratification at mid-cavity height remained very close to 1 for Ra_H values up to 2×10^9 and increased to 1.2 for 10^{10}. The increased stratification is attributed to an increased depth of the isothermal hot

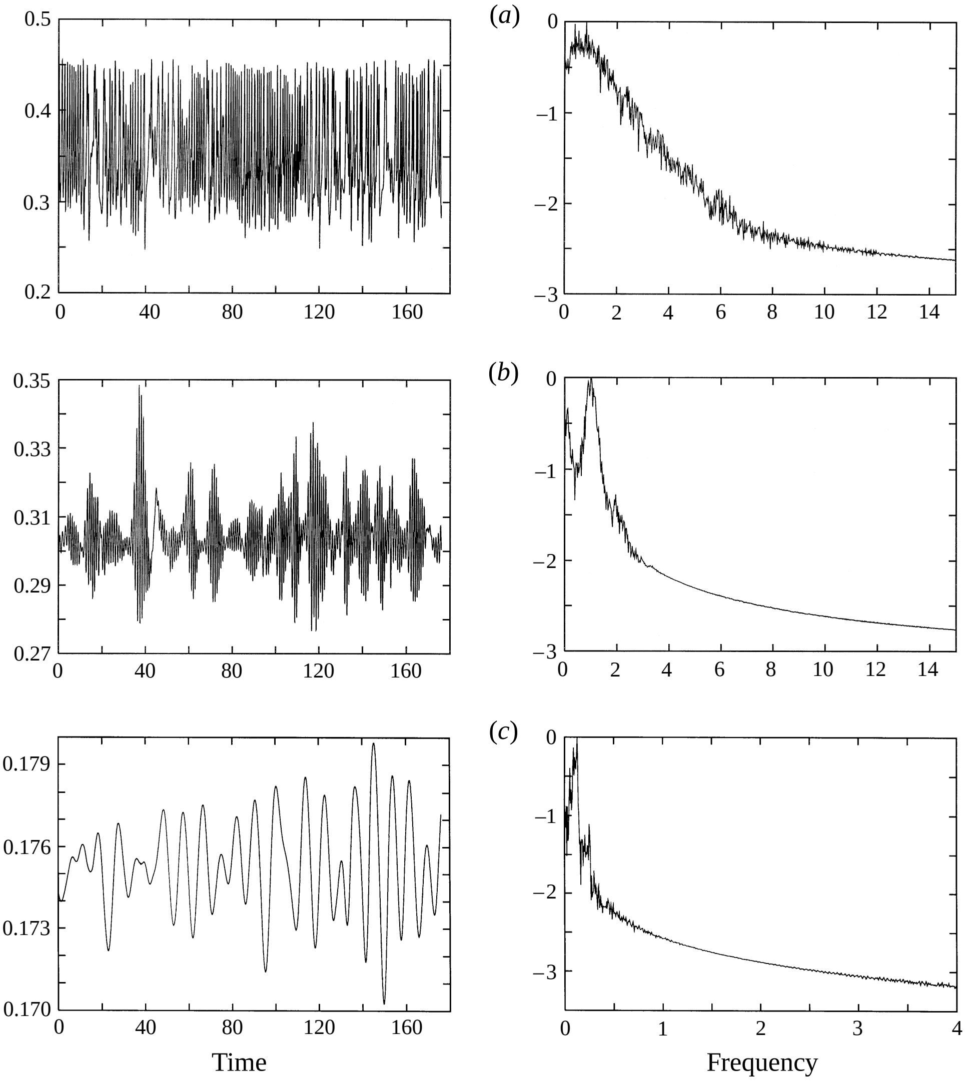

FIGURE 18. Time traces of temperature (left) and their density power spectra (right) at locations $(x, z) = (0.0054, 0.85)$ (*a*), $(x, z) = (0.0054, 0.735)$ (*b*), $(x, z) = (0.0054, 0.5)$ (*c*) for $Ra = 10^{9.5}$. Spatial resolution 256×384, calculation performed with $\Delta t = 1 \times 10^{-3}$. The first two density power spectra have been obtained from averages of 4 spectra of 2048 points each over a time interval of 40.96.

and bottom parts of the core as a result of enhanced mixing, which in turn results in an increased slope near the mid-cavity height. Our results are further confirmed by some more recent results by Nobile & Sousa (1994) showing the same trend (i.e. stratification larger than 1). Therefore, there is no evidence of stratification decrease in this range of *Ra*, and the low value reported by Paolucci (1990) was probably due to insufficiently long integration, particularly in the light of his computation being performed from rest. As is evident, the time-averaged isotherms in the core are straight horizontal lines and no longer show the wave-like patterns discussed previously. This is further evidence of their internal wave origin.

Ra	f	$f \times Ra^{-1/4} \times 10^3$	Nu	$NuRa^{-1/4}$
10^8			30.2	0.302
3×10^8	0.55	4.12	40.1	0.305
10^9	0.75	4.22	54.6	0.307
$10^{9.5}$	1.0	4.22	74.5	0.310
10^{10}	–	–	100	0.316

TABLE 3. Travelling wave frequency f and Nusselt number Nu.

3.5.2. *Instantaneous flow features*

For the sake of brevity, only examples of time traces of temperature for $Ra = 10^{9.5}$ at several locations in the upward boundary layer are displayed in figure 18. At the mid-cavity height, the time trace of the temperature exhibits low-frequency oscillations which correspond to the internal wave oscillations. Further downstream, at $(x, z) = (0.0054, 0.735)$ one begins to see travelling waves which appear as high-frequency oscillations modulated by a smaller frequency. The high frequency corresponds to the travelling waves in the boundary layers and the peak frequency obtained from a density power spectrum of the signal is equal to 1.0. At a position further downstream $(x, z) = (0.0054, 0.85)$, the waves have grown resulting fluctuations of much larger amplitude which are also much more irregular in time.

Table 3 shows the evolution of basic frequencies found in the typical time traces of pointwise quantities as the Rayleigh number increases. In particular, it is clear that the high-frequency characteristic of the travelling waves evolves like $Ra^{1/4}$. This behaviour is somewhat surprising since it has been previously shown (Penot *et al.* 1990) that, for the travelling wave instability, each individual branch of solution is characterized by a constant frequency in the units considered here. The explanation is the following: since we are considering a wide range of Rayleigh numbers, we are not observing the dependence of the frequency of the oscillations on one single solution branch but the evolution with Ra of the characteristic frequency of several of them. Previous linear stability analysis of the buoyancy layer by Gill & Davey (1969) has indicated that the ratio of the phase speed of the travelling waves to the maximum velocity is constant and approximately equal to 0.8. Since the maximum velocity itself is constant (in the velocity units considered here), the decrease in frequency is linked to the increase of the number of travelling waves circulating around the cavity. Assuming that the ratio of the wavelength of the travelling waves to the boundary layer thickness remains constant, the number of waves scales like the reciprocal of the boundary layer thickness which decreases like $Ra^{-1/4}$, accounting for the observation. This suggests that, at least for the range of Ra in the table, the classical laminar scalings still hold regardless of the chaotic nature of the flow.

3.6. *Sample turbulent statistics*

One of the promising features of these 'direct numerical simulations' is the possibility of computing the average quantities which characterize the turbulent motion. It should be emphasized that, since the corresponding flows are only transitional, the quantities presented in this section should be considered more as a check of the methodology rather than actually physical turbulent quantities. As noted in the Introduction, realistic turbulent quantities can only be obtained from three-dimensional computations. For $Ra = 10^{9.5}$ examples of such calculations for turbulence kinetic

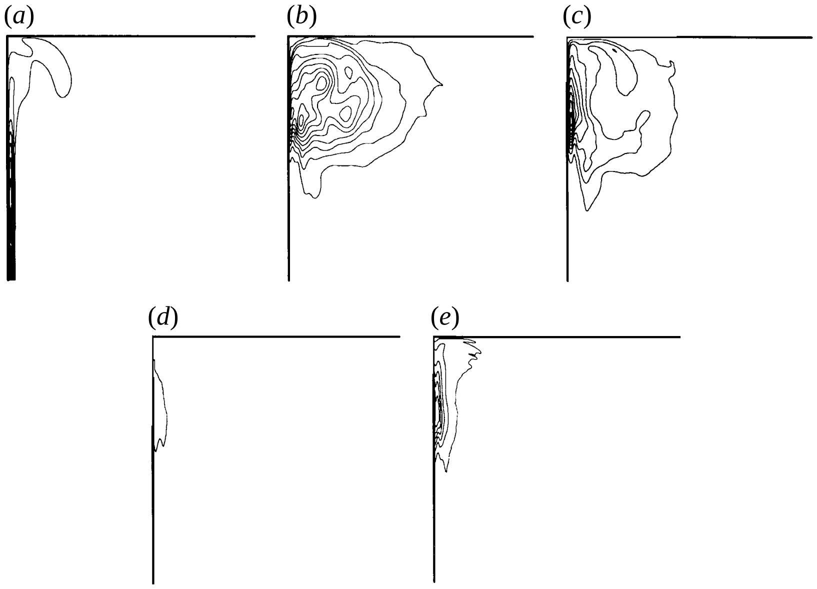

FIGURE 19. (*a–e*) Turbulent fields for $Ra = 10^{9.5}$: (*a*) mean kinetic energy, (*b*) turbulent energy $\frac{1}{2}\overline{u_i'^2}$, (*c*) temperature variance $\overline{\theta'^2}$, (*d*) viscous dissipation $\overline{(\partial u_i'/\partial x_j)(\partial u_i'/\partial x_j)}$, (*e*) thermal dissipation $\overline{\partial \theta'/\partial x_j)(\partial \theta'/\partial x_j)}$. Only the upper left quarter of cavity is shown.

energy of the mean motion, the temperature variance, and the viscous and thermal dissipation rates are displayed in figure 19. These plots nonetheless confirm that, as previously noted, turbulent fluctuations are only significant in the downstream part of the boundary layer. They also show that the temperature fluctuations are spatially well correlated to the thermal dissipation rate, but this does not seem to hold so well for the turbulent energy and its viscous dissipation. For the higher *Ra* value of 10^{10}, similar trends have been observed (Le Quéré 1994).

3.7. *Heat transfer*

Table 3 also gives a comparison of the time- and space-averaged Nusselt numbers for different *Ra* values. For the sake of completeness we also recall the value obtained for 10^8 (Le Quéré 1991). The last column shows that over the range of *Ra* values considered, a $Nu \propto Ra^{1/4}$ relationship is still valid, which shows that, at least for the range considered here, the chaotic motion has only a minor influence on the mean heat transfer. Typical local Nusselt number distributions are shown in figure 20. They show that the chaotic motion only plays a significant role in the downstream part of the boundary layers since the time envelopes of the local maximum and minimum Nusselt numbers are identical for up to about $z \simeq 0.7$. It is also apparent that there is a region of exponential growth of the fluctuations in the boundary layer. This region moves upstream with increasing Rayleigh number. The value at which this rapid growth is observed is consistent with what was found experimentally by Mergui & Penot (1996). In fact, the shape of their measured local Nusselt number profiles is very similar to ours, despite the fact that their temperature boundary conditions are different. We note that their boundary conditions are more representative of the perfectly conducting case whereas our horizontal walls are adiabatic. Given this difference, the agreement between our results interpolated for $Ra = 1.69 \times 10^9$, that

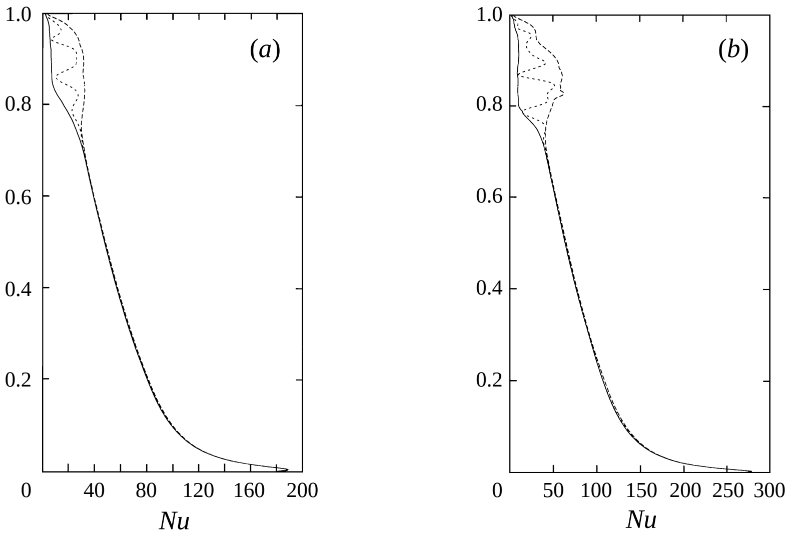

FIGURE 20. Local Nusselt number distributions along hot wall for $Ra = 10^9$ (*a*) and $Ra = 10^{9.5}$ (*b*). Solid and dashed lines are the maximum and minimum envelopes in time while the dotted line is a typical instantaneous distribution.

is 62.5, and their measured values of 53 and 56 along the heated and cold walls, respectively, is fair.

4. Conclusion

We have performed two-dimensional computations of natural convection in a differentially heated square cavity starting from the onset of unsteadiness to the transitional chaotic regime. These computations have been carried out with a code based on Chebyshev spatial differencing and a second-order time-stepping algorithm and are thus believed to be highly accurate. In particular we have paid attention to the time integration lengths in order to obtain the asymptotic time behaviour of the solutions, both at the onset of unsteadiness and for the chaotic regime in order to obtain meaningful statistical quantities. We have shown that the onset of unsteadiness takes place at a critical $Ra = 1.82 \times 10^8$ and that the first instability mode breaks the usual centro-symmetry of the solution. This instabilty takes place at the base of the detached flow region along the horizontal walls. The boundary layers themselves become unstable soon after, and transition to chaos seems to proceed through quasi-periodicity. Concerning the chaotic regime, we have shown that the time-averaged flow structure increasingly departs from the classical laminar structure, although the laminar scalings still hold. The vertical stratification in the core region remains larger than 1 for the range of parameters considered here. It is hoped that extension of such computations to larger Rayleigh numbers and three dimensions will serve to contribute to the establishment of a data base which will help the development of better turbulence models for buoyant flows.

The computations were performed on the CRAY-2 at C2VR and on the C90 at IDRIS. This work was supported by DRET under contract 91-150. M. Behnia acknowledges CNRS's partial financial support during his stay at LIMSI.

REFERENCES

Armfield, S. 1992 Conduction blocking effects in stratified intrusion jets. In *Proc. 11th Australasian Fluid Mech. Conf.*, pp. 335–339.

Chossat, P. 1984 Bifurcations en présence de symétrie dans les problèmes classiques de l'hydrodynamique. *J. Méc. Théor. Appl.* Special issue, 157–192.

Fromm, J. E. 1971 Numerical method for computing non-linear, time-dependent, buoyant circulation of air in rooms. *IBM J. Res. and Development*, pp. 186–196.

Gill, A. E. & Davey, A. 1969 Instabilities of a buoyancy driven system. *J. Fluid Mech.* **35**, 775–798.

Haidvogel, D. & Zang, T. 1979 The accurate solution of Poisson's equation by expansion in Chebyshev polynomials. *J. Comput. Phys.* **30**, 167–180.

Haldenwang, P. 1984 Résolution tridimensionnelle des équations de Navier–Stokes par méthodes spectrales Tchebycheff. Thèse d'Etat, Université de Provence.

Henkes, R. A. M. W. 1990 Turbulent natural convection boundary layers. PhD thesis, University of Delft.

Janssen, R. J. A. & Henkes, R. A. W. M. 1994 Stability of the natural convection flow in differentially heated rectangular enclosures with adiabatic horizontal walls. *First ERCOFTAC Workshop on Direct and Large Eddy Simulation* (ed. P. Voke). University of Surrey.

Le Quéré, P. 1987 Etude de la transition à l'instationnarité des écoulements de convection naturelle en cavité verticale différentiellement chauffée par méthodes spectrales Chebyshev. Thèse d'Etat, Université de Poitiers.

Le Quéré, P. 1991 Accurate solutions to the square thermally driven cavity. *Computers Fluids* **20**, 29–41.

Le Quéré, P. 1994 An improved Chebyshev collocation algorithm for direct simulation of 2D turbulent convection in differentially heated cavities. In *Proc. ICOSAHOM Conf., Montpellier, France.*

Le Quéré, P. & Alziary de Roquefort, Th. 1985 Computation of natural convection in two-dimensional cavities with Chebyshev polynomials. *J. Comput. Phys.* **57**, 210–228.

Mergui, S. & Penot, F. 1996 Convection naturelle en cavité carrée différentiellement chauffée: investigation expérimentale à $Ra = 1.69 \times 10^9$. *Intl J. Heat Mass Transfer* **39**, 563–574.

Nobile, E. & Sousa, A. C. M. 1994 An implicit scheme for the numerical simulation of time-dependent convection is side-heated cavities. In *Transient Thermal Hydraulics, Heat Transfer, Fluid Structure Interaction and Structural Dynamics: ASME Pressure Vessels and Piping Conf., Minneapolis, MN*. ASME PVP, vol. 270, pp. 29–37.

Paolucci, S. 1990 Direct simulation of two-dimensional turbulent natural convection in an enclosed cavity. *J. Fluid Mech.* **215**, 229–262.

Paolucci, S. & Chenoweth, D. R. 1989 Transition to chaos in a differentially heated vertical cavity. *J. Fluid Mech.* **201**, 379–410.

Patterson, J. & Imberger, J. 1980 Unsteady natural convection in a rectangular cavity. *J. Fluid Mech.* **100**, 65–86.

Penot, F., Ndame, A. & Le Quéré, P. 1990 Investigation of the route to turbulence in a differentially heated cavity. In *9th IHTC*, vol. 2, pp. 417–422.

Ravi, M. R., Henkes, R. A. W. M. & Hoogendoorn, C. J. 1994 On the high-Rayleigh number structure of steady laminar natural-convection flow in a square enclosure. *J. Fluid. Mech.* **262**, 325–351.

Thorpe, S. A. 1968 On standing internal gravity waves of finite amplitude. *J. Fluid Mech.* **32**, 489–528.

Tritton, D. J. 1988 *Physical Fluid Dynamics.* Oxford Science Publication.

Vahl Davis, G. de & Jones, I. P. 1983 Natural convection in a square cavity: a comparison exercise. *Intl J. Numer. Meth. Fluids* **3**, 227–248.

Xin, S. & Le Quéré, P. 1995 Direct numerical simulation of two-dimensional chaotic natural convection in a differentially heated cavity of aspect ratio 4. *J. Fluid Mech.* **304**, 87–118.